Variability of the Indo-Pacific Ocean Exchanges

Carl Wunsch

Department of Earth, Atmospheric and Planetary Sciences

Massachusetts Institute of Technology

Cambridge MA 02139 USA

email: cwunsch@mit.edu

November 29, 2009

Abstract

The ECCO-GODAE global estimate of the ocean circulation 1992-2007 is analyzed in the region of the Indonesian Throughflow (ITF), including the Southern Ocean flow south of Australia. General characteristics are an intense month-to-month noise, only weak trends, and an important annual cycle (which is not the focus of attention). Apart from the details of the unresolved flows within the various passages, and right on the equator, the region and its large-scale climate effects appears to be accurately diagnosed by large-scale geostrophic balance, so that the ITF can be calculated either from the upstream or the downstream balanced flow (but no simple reference level can be defined). The INSTANT program occurs during a more or less typical three-year period. Indications of response to the large 1997-1998 El Niño are weak.

1 Introduction

The Indonesian Throughflow (ITF) is simultaneously a consequence of, and control on, the global ocean circulation. As such, it must be understood in a global context. This region displays some

of the most intricate of oceanic flows and is not simple to describe in space or time. Involved are the physics of mid- and low-latitude, and equatorial flows, strong topography and possibly hydraulically controlled straits, intense tidal and other mixing, and the volatile disturbances of the general low-latitude ocean. The Volume 101, C5, May 1996 special issue of the *Journal of Geophysical Research* contains numerous papers describing the ITF, the observations available at that time, and their interpretation. Review articles by Godfrey (1996), Meyers (1996), and the hydrographic discussion of Fieux et al. (1996) prove particularly helpful in what follows. Gordon (2005) provides a semi-technical overview of the problems. McCreary et al. (2007) is a convenient starting point for references on the modeling issues. Gordon et al. (2008) and Sprintall et al. (2009) describe the recent measurements within the individual passages in the INSTANT (International Nusantra Stratification and Transport) program. (This reference list is incomplete, and this paper is not intended as a comprehensive revie-.)

Here we use the so-called MIT-AER ECCO-GODAE[1] estimates of the global circulation to estimate the mean and variability of the ITF over the period 1992-2007. These estimates (see Wunsch and Heimbach, 2007, 2009) are the result of the least-squares fit of an evolved ECCO version of the MITgcm (Marshall et al., 1997) to the great variety of the global scale data sets available during that period. Data include the altimetry from all extant missions, Argo floats, CTDs, XBTs, elephant seal temperature profiles (SeaOS), etc., all weighted according to best available estimates of their various errors. The particular configuration, called version 3, differs from its predecessors in numerous ways, of which the most significant are probably the employment of a full sea ice sub-model, which greatly modifies the details within the Southern Ocean, and use of atmospheric state variables and bulk formulas for the surface boundary conditions. A full account will be published elsewhere. Readers unfamiliar with state estimation methods need only know that the model physics are dominated almost everywhere by the thermal

[1] Massachusetts Institute of Technology—Atmosphere Ocean Research Estimating the Circulation and Climate of the Ocean—Global Ocean Data Assimilation Experiment

wind balance, with local flows indistinguishable from geostrophy except in very specific places where higher order physics must enter. Model solutions are freely running with none of the artificial sources or sinks of momentum or heat, etc. that are commonly introduced by other estimation methods, and they are thus useful for budget calculations. The main data issue directly pertaining to the Indonesian archipelago is the suppression of altimetric data everywhere from water depths less than 1000m. In the Indonesian region, in particular, the shallow water tidal corrections to altimetry are known to contain errors generally larger than elsewhere.

As part of the estimation method, differences and misfits to every one of the observations are computed. Here "misfits" are defined to be the squared difference between the model calculated value of a quantity (e.g., salinity) and its observed value, normalized by the variance of the expected error. A full description requires an elaborate discussion of each data type (e.g., Ponte et al., 2007; Stammer et al., 2007; Forget and Wunsch 2007). We show here, as representative of the much larger data sets, the global distribution of the the vertical integral of the misfit to the Argo float data, and the difference between the model and the altimeter data averaged over 16 years (Figs. 1, 2). The latter is given in unweighted, unsquared, form so as to display the magnitudes, and signs, of the differences that underlie the formal misfits. These figures are meant to convey the scope of the regional and global coverage of two of the main data types, as well as showing the degree of consistency achieved. A full discussion of the data and global results must be left to the references.

As compared to previous discussions of the ITF, the advantage here is the ability to describe the region with a uniform dynamical framework over 16 years, and to employ data sometimes remote from the region itself as constraints, because fluid flows connect over remote times and distances. Variability can be described on all time scales from about two months out to 16 years, thus including sub-seasonal, seasonal, and interannual variability and for which the physics can be expected to be distinct. The flow fields are also consistent with the known model

equations and remove the need to rely upon arbitrary level-of-no-motion assumptions. In some elements, none obviously visible in this region, the solutions exhibit transient behavior near the beginning and end of the estimation period. Transients arise from the absence of data prior to and following the estimation interval, and for the most recent years, a much shortened set of optimization iterations after the data were introduced.

None of the INSTANT data were used in the estimates—because they became available very late in the effort, are purely regional, exist in passages sometimes unresolved by the model, and span a fragment of the ECCO-GODAE estimation period. We do succeed in providing some context for their interpretation.

This note is not intended as a comprehensive account of the ECCO-GODAE solutions, nor of the tropical Indo-Pacific. The intent is a primarily kinematic description of the temporal variability in the region. It may be unique in its attempt to use all of the global oceanographic data and a global GCM to estimate what is happening there. From the point of view of the ECCO project, the collective focus in this special journal issue on the ITF is an incentive and opportunity to obtain reassurance (or otherwise) of the realism of the estimates made independently in an interesting area of the ocean. A full discussion is not possible in a comparatively brief paper: it would involve the full depth behavior of the three components of velocity, temperature, salinity, pressure, and the adjusted meteorological fields—two components of wind stress, enthalpy and freshwater exchanges and their mutual relationships on al time scales. In particular, the strong annual variability is mainly being ignored as it has been the focus of attention by others, although largely in models, and because its analysis is necessarily different from that in other frequency bands where there is no strong deterministic forcing.

Before proceeding, a few numbers for scale are helpful. Suppose that an oceanic region 1000km on a side is subject to a net inflow-outflow imbalance of 1 Sv ($= 10^6 \mathrm{m}^3/\mathrm{s}$). Then if sustained for one year, mean sea level over the region would change by about 30m. Empirically,

one observes large-scale sea level changes over a year of 10cm at most. Thus one anticipates volume transport divergences can be no more than roughly 0.03Sv for a year. It would thus be unsurprising to find ITF-region volume imbalances no larger than a few tenths of a Sv for a few months.

To provide a bit of context, Fig. 3 shows the Southern Oscillation Index (SOI) from 1992 through 2007. The very large El Niño of 1997-1998 appears as a sustained negative anomaly, with a short-lived but intense negative feature appearing in 2005.

2 Some Geometry

Somewhat arbitrarily, the domain shown in Fig. 4 will be used for the analysis. The resolution of the particular ECCO estimate (numerous ones exist), version 3.73, is 1° of latitude and longitude, which is too coarse to be regarded as providing an accurate rendering of the local dynamics through these complex passages. Thus the Lombok and Torres Straits are closed, with the net flow pathway forced to go via the Banda Sea outlet.[2] Nonetheless, because the model is tightly constrained to various observations in the surrounding Indian and Pacific Oceans, and because geostrophic balance dominates, the result assures that volume and water mass characteristics of the entering Pacific flow are consistent with the exiting Indian Ocean flow. Consistency with the large-scale geostrophic balance means that the net advective exchanges of enthalpy, salt, and mass will be accurately calculated—even if the governing momentum, energetics and mixing within the passages are inaccurate in detail.

[2] The representation of unresolved topography in all coarse resolution GCMs is something of an art. Lu et al. (2002) describe the manipulation of the shape of various narrow passages in the ECCO model, so that approximately 11Sv was produced in the ITF before data-fitting. That a wide range of temporal variability in transports results in the estimates here suggests that the topographic shape is important but not wholly determining. The skill in computing mean transport properties independent of manipulation of the topography is obscure in all GCMs.

To produce a digestible data set, the four meridional sections through the area shown in the figure will be used for a more detailed analysis. The section at the western edge (1) is adjacent to the Ninety-East Ridge and when its transport is integrated from south to north, it captures the entire zonal flow in the world ocean—including the eastward-going Antarctic Circumpolar Current (ACC) and the westward flow across the total Indian Ocean. Sections (2) and (3) are split by Australia and in the north (2B, 3B) cut across the ITF. Section 2B, which will be the focus, slices across the South China Sea and intersects the Australian coast at 114.5°E just west of the Lombok Strait and the pair of hydrographic sections discussed by Fieux et al. (1996). For some purposes (the heat transport), 2B is sub-divided into 2B′ (Australia to Borneo), and 2C, across the South China Sea. In the south, the sections 2A and 3A depict what we will label the "South Australian Throughflow" (SAT), and which includes, but is not restricted to, the Antarctic Circumpolar Current. The analysis is of the monthly means, albeit much additional high frequency variability is suppressed that way.

3 Top-To-Bottom Volume Transport

The top-to-bottom zonal volume transports (the model is currently configured with the Boussinesq approximation) are a limited but nonetheless useful initial representation of the results. Define them with the symbols, U_{2A}, U_{4B}, etc. Then U_{2A}, $U_{3A,}$ U_{4A} are nearly identical, as anticipated (a few tenths of a Sverdrup differences) implying small volume storage terms. We will thus display U only from 1, 2A, 2B and shown in Fig. 4. (Subsections such as $4B$ were defined to permit mass-conserving heat transport calculations, but only touched on below.) The time mean of the ITF, defined as $U_{2B} = -11.5 \pm 2.4$Sv (negative meaning westward), $U_{2A} = 155 \pm 5$Sv and for $U_1 = 143 \pm 4$ (all error estimates here are simple temporal one-standard deviations, the systematic errors being unknown). That is, as expected, $U_1 = U_2 = U_{2A} + U_{2B}$ almost exactly, as mass conservation requires. For comparison the "snapshot" estimate by Ganachaud (2003) from

a global inverse calculation using one of the Fieux et al. (1996) sections, produced an equivalent to $U_{2B} = -16 \pm 5$Sv, and which is consistent within uncertainy estimates with the ECCO 16-year mean. Other values summarized by Gordon (2005) lie in the range of -9 to -11Sv. The ECCO maximum *westward* monthly flow is 17.4Sv and the minimum is 6.6Sv. Sprintall et al. (2009) calculate a three-year average value of -15Sv from direct measurements in the passages, but they quote a possible range, arising from systematic errors of extrapolation, from -11 to -19Sv, to which would be added the stochastic errors, and so there is no numerical conflict. A histogram of U_{2B} is shown in Fig. 5 (the South China Sea volume flux nearly vanishes and so U_{2B} is almost identical to $U_{2B''}$). A very broad distribution is apparent with a hint that the average value is not the most common one—perhaps reflecting a tendency toward bimodality in El Niño/La Niña states. If so, the effect is subtle. The strong time dependence here means that the importance of the time-mean is not so clear and that data durations of less than many years may well be unrepresentative of climatological values.

Fig. 6 shows the 16-year time-average zonal flow in Section 2B, running from the north coast of Australia to the Indonesian archipelago and then across the South China Sea. A strong westward flow near-surface along the Indonesian coast (the South Equatorial Current) is visible, but much of the rest of the flow extends to depth with no simple reference level visible. (There is a very small eastward flow in the shallow area just south of Borneo, barely visible in the plots.) No eastward flow, in what is called the South Java Current (e.g., Meyers, 1996), is apparent. The reversals at depth into eastward flow are weak but stable.

To portray some of the nature of the temporal variability, Fig. 7 shows the August flow in four different years four years apart. Below the surface a complex of spatially reversing structures occur that are not easy to summarize. Discussion of the tranports using a fixed geostrophic reference level will be problematic (see e.g., Wijffels et al., 2008). An equivalent display of four February snapshots (not shown) has stronger near-surface *eastward* flows in some

years. Clearly the flow is highly baroclinic and it seems unlikely that it can be diagnosed e.g., by simple surface elevation differences.

Figs. 8, 9 shows the general noisiness of the volume fluxes with a visually obvious, but somewhat irregular, annual cycle. The existence of the large El Niño episode of 1997-1998 is not readily apparent. It does coincide with a local minimum in the total zonal transports, but one of no particular extreme. The ITF shows a small strengthening at that time, extending for about the next four years. But it is not possible to say whether it was a consequence of the ENSO cycle or merely an ordinary low frequency fluctuation from random superpositions, and of no specific cause. In any case, it is a weak feature and similar ones of similar duration occur both before and afterwards.

Estimates of the power densities of these records are shown in Fig. 10. Overall shape is consistent with a weakly red-noise character having a superimposed annual cycle containing about 50% of the variance over 16 years. The annual cycle is broadband in character, and is not a pure frequency—rather it is a superposition of a band of frequencies around one cycle/year. U_{2A} contains a weak semi-annual energy excess. Linear predictability of these volume transports at periods beyond a year is controlled by the slope of the spectral density, given approximately by the power law s^{-q}, where s is the frequency. Steeper q produces larger predictability. A least-squares fit to the transport of U_{2B}, at periods longer than about two years produces $q \approx 0.35 \pm 0.07$ and the transport variability is thus barely distinguishable from white noise—which has no linear predictability. The slope carries implications for the statistical properties of any empirical trend determination (see e.g., Percival, et al., 2001). Note, however, that the low frequency spectral slope estimate is one aspect of spectral analysis particularly sensitive to the methodology. The spectra in Fig. 10 are multitaper estimates (e.g., Percival and Walden, 1993) and which are known to be biased low at the lowest frequencies. Estimates based upon the periodogram and a Daniell window (not shown), have a considerably steeper slope (close

to $q = 1.5$) in the lowest resolved frequencies. Linear predictability is much greater for such records, but a definitive determination of the slope is not possible over such a short interval.

The coherence between the ITF and SAT transports is shown in Fig. 11. They are strongly coherent in the annual and semi-annual bands (unsurprising), but do not show any statistically significant coherence at periods longer than one year. The phase stability seen at these low frequencies, however, suggests that there is some true coherence, but accounting for less than about 25% of the variance, and having a phase of about 180°—as mass conservation would suggest and as reflected in the power densities in Fig. 10.

4 Relation to Pressure

There has been speculation that the ITF is "driven" by the pressure difference between the Pacific and Indian Oceans (e.g., Wyrtki, 1987, Meyers, 1996 and see Kamenkovitch et al., 2009). As with any time-mean flow, the Bernoulli relationship requires that the current flow "downhill" (see the discussion by Montgomery, 1941, of the situation in the Gulf Stream) and one expects to see a slight pressure drop following the mean streamlines. As the elevations change in the western Pacific and eastern Indian Ocean through responses to the wind and other forcing, and the very large changes associated with the ENSO cycle, one might anticipate fluctuations in the pressure head to be associated directly with those in transport.

On the other hand, the situation is complicated by the strong tendency even for flows very close to the equator to be in geostrophic balance (e.g., Eriksen, 1981; Fieux et al., 1996). In geostrophy, one cannot claim the pressure gradients drive the flow any more than that the flows drive the pressure differences. The question here then is whether there are some simple kinematic relationships that might shed some insight on the connection of the elevation and flow fields beyond the inference that the non-equatorial flows are indistinguishable from geostrophic ones? The context of any discussion is the large-scale dynamic topography, shown in Figs. 12 and

13, and which will control the time-mean flow in the region surrounding the ITF. Except right on the equator, one expects no detectable deviation from geostrophic balance, and hence the ITF itself must be consistent with the divergences of the complex mean flow in the surrounding area.

In some of the global empirical orthogonal functions discussed by Wunsch and Heimbach (2009), the 1997-1998 El Niño is visually quite pronounced. Perhaps surprisingly, Fig. 8 does not display any very impressive evidence of that huge event (recall Fig. 3) and the height differences (see Fig. 14) are almost entirely due to the annual cycles (a result shown, e.g., by England and Huang, 2005 or Potemra and Schneider, 2007). If the records are reduced to annual averages, the 1997-1998 interval is seen, as already described, to coincide with the beginning of a general increase in westward transport lasting about four years. The coherence (Fig. 15) between the east-west pressure gradient and the low frequency variations in U_{2B} is marginally significant and at best accounts for only a small fraction of the variation. Little more can be said.

5 Relation to the Wind Field

The wind field is the most obvious control on oceanic flows. In the time-mean winds (not shown), bands of easterlies and westerlies are apparent in τ_x including a reversal across the Indonesian archipelago. τ_y is generally weaker than τ_x, with another set of sign reversals with latitude.

The spatial average of τ_x was formed over an eastern box from 136.5°E to 143.5°E and a western box from 91.5 to 114.5°E, both extending from 20.5°S to 14.5°N, and shown in Fig. 16. Fig. 17 shows the coherence between U_{2B} and τ_x averaged over the boxed regions. The difference of these two spatial average wind fields does show a visual ENSO signal.

Coherence amplitude approaching 0.8 is apparent at low frequencies, implying an explained variance near 60% with a phase lag indistinguishable from zero. Thus much of the low frequency

variability appears to be forced by fluctuations in the wind field over the western Pacific Ocean. The annual cycle and its harmonics are also coherent.

All parts of the fluid ocean are ultimately coupled, although the time for a remote disturbance to propagate into the ITF can be very long. As an indication of the way in which remote components of the wind field are capable of influencing the volume transport, Fig. 18 displays the sensitivity of U_{2B} to perturbation disturbances in the zonal wind field at successively *earlier* times. This result is taken from Heimbach et al. (2009) which should be consulted for details. For present purposes, it must suffice to say that it is based upon the adjoint solution used in the ECCO optimizations. As expected, the dominating, most recent, sensitivity is to the wind within the equatorial band, with some coastal regions capable of rapid communication with the ITF showing secondary effects. Potemra and Schneider (2007) show a similar result at 3 months (their Fig. 7). When disturbances occur further back in time, the dominating regions expand off the equator, losing point-wise importance, but extending eventually over very large areas of influence. A full discussion of these and similar results for other disturbance fields is beyond the scope of the present paper.

6 Enthalpy Transport

Variations in the temperature transport are of considerable interest, and their analysis presents a physically meaningful way of upweighting the flow in the upper ocean, where the relatively shallow passages are most important. Unlike the volume transport divergences, significant heat transfers to and from the atmosphere are possible regionally. (Wunsch and Heimbach, 2009, show that the global meridional heat transport properties of this solution are consistent with direct, independent, estimates.) Time- and latitude-averaged temperature profiles of some of the subsections are seen in Fig. 19, and show the near exponential upweighting of the upper ocean flows that take place in the temperature transport calculations. Fig. 20 shows the time series of

temperature transport, T_j, in the ITF sub-sections, as well as T_{2A} and T_1. The great volatility in the ITF transports is suppressed in T_{2A}, showing that the fluctuations in T_1 originate in the low-latitude components.

Fig 20 shows the monthly temperature transports in °C Sv. (In a volume-conserving system, 1°C Sv$\approx 4 \times 10^{12}$W, so that 500°C Sv would be about 2PW. Because this system has a net throughput, only the divergences are meaningful.) The Southern Ocean contributions are far more temporally stable than are the ITF or South China Sea contributions. Visually, the predominant character is one of great noisiness on all time scales. The time-means of the temperature transports across each of the sections is 265±269 (T_1), 265±81 (T_2), 235±16 (T_3), 201.2±269 (T_4) °C Sv (including the SAT). The mean temperature transport in the ITF alone, $T_{2B'} = -202 \pm 170$°Sv, or $-(8 \pm 7) \times 10^{14}$W if converted using a reference temperature of O°C. (Gordon, 2005, quotes previous estimates between $-$ (5 to 10) $\times 10^{14}$W.) Fluctuations are again very large.

7 Fresh Water

Temporal variability of the salt transport is essentially the same as the volume transport. Because the system is open, only the salt divergences are interpretable. Fig. 21 displays the annual average salt divergences between sections 2B and 3B ($S_{2B}-S_{3B}$), and $S_{3B}-S_{4B}$. On average, both are positive (net influx of salt from the east), and consistent with balance maintained here by net precipitation. (Note that the latitude span here is very large.) The mean values are equivalent to a net precipitation of 0.05±Sv in both regions (compare to Trenberth et al., 2007, Fig. 3). Fig. 22 shows the adjusted time-mean net precipitation in the ECCO estimate (meteorological forcing is part of the ECCO control vector, and is thus adjusted during the least-squares fitting). Among other complications, this region is apparently one of strongly spatially (and temporally—not shown) variability in the net precipitation.

8 Discussion

The ECCO-GODAE estimates of the ITF volume transports are consistent with the emerging consensus of a time mean near -11.5 ± 2.4Sv, with only minor ENSO contributions. More important, however, is that the month-to-month variability in both volume and temperature transports is very large, and interannual fluctuations are also considerable. Finding that the ENSO contribution is a comparatively minor component of the ITF is compatible with the inferences of a number of previous authors, including e.g., England and Huang (2005; primarily a modeling study resulting in a 10% of the variance from ENSO) and Potemra and Schneider (2007) and the references found there. Although perhaps intuitively unexpected, this result appears to be a strong one.

The problem of determining long-term average values, of primary interest in climate studies, from short records will be apparent. Local wind forcing variations are the most direct and obvious cause of variability of the ITF, but as the ITF represents a summation of both local, immediate, influences and distant, past changes, no simple quantitative statement about changes on all time scales has proven possible.

Although no specific tests have been run, the INSTANT data appear, from the wider spatial and longer duration ECCO-GODAE estimates, to have been obtained during a not untypical period of time. No unusual features are visually evident in the records during INSTANT.

That the ECCO estimate, which does not yet resolve the Indonesian passages, produces results indistinguishable within uncertainties from the short-lived direct passage monitoring, has some important consequences. Geostrophic relations are controlling almost everywhere, and the flow and its properties entering and leaving the Archipelago must be balanced. Because net water storage effects are slight, geostrophy in either the western Pacific or eastern Indian Oceans is a good diagnostic of the ITF itself. To the degree that the detailed physics of the passages determines the upstream and downstream flows, that is controls the distant geostrophic balance

(unclear), it is irrelevant to the problem of calculating the ITF. Only the larger scale geostrophic flow must be known—something that the ECCO system does robustly (it is the dominant balance of the model almost everywhere; the space/time covariance of the surface pressure gradient and the zonal flow across section 2A produced an estimated correlation coefficient exceeding 0.99). The temperature and salinity contents of the ITF are presumably controlled in part by mixing and higher order physics within the passages. As with the volume flux, the water mass properties both entering and leaving the archipelago are well-determined by the ECCO system. Details of the mixing and flow control with the various Straits, however interesting, are of no particular large-scale consequences to determining the inter-ocean transfers. Predicting changes under changed climatic conditions is a very different problem—not undertaken here.

If the ocean circulation is undergoing significant climate trends in this region, they are difficult to perceive with the data available. On the other hand, given the noisiness of the results, such trends would have to be considerable to be deemed significant in the presence of what appears to be red noise processes. Far longer records will be required to understand secular change in the ocean (see also Wunsch and Heimbach, 2009, for a global variability discussion).

Note on model output: The estimated solution discussed here is publicly available and its use encouraged. See http://ecco-group.org/, or contact the author for assistance.

Acknowledgements. Supported in part by the National Ocean Partnership Program (NOPP), NASA, and NOAA through the Geophysical Fluid Dynamics Laboratory (GFDL). Computations have been carried out both at GFDL and the National Center for Atmospheric Research, which is supported by the National Science Foundation Thanks are owed all the ECCO consortia members. Comments by A. Gordon were very helpful as were numerous corrections suggested by the anonymous reviewers..

References

England, M. H., and F. Huang, 2005. On the interannual variability of the Indonesian throughflow and its linkage with ENSO, J. Clim., 18, 1435–1444.

Eriksen, C.C., 1981. Deep currents and their interpretation as equatorial waves in the western Pacific Ocean. J. Phys.Oc., 11, 48-70.

Fieux, M., Molcard, R. and Ilahude, A.G., 1996. Geostrophic transport of the Pacific-Indian oceans throughflow. J. Geophys. Res, 101, 12421-12432.

Forget, G. and Wunsch, C., 2007. Estimated global hydrographic variability. J. Phys. Oc. , 37, 1997-2008.

Ganachaud, A., 2003. Large-scale mass transports, water mass formation, and diffusivities estimated from World Ocean Circulation Experiment (WOCE) hydrographic data. J. Geophys. Res, 108,

Godfrey, J.S., 1996. The effect of the Indonesian throughflow on ocean circulation and heat exchange with the atmosphere: A review. J. Geophys. Res, 10, 12217-12237.

Gordon, A. L., 2005. Oceanography of the Indonesian Seas and Their Throughflow. Oceanography, 18, 14-27.

Gordon, A., Wijffels, S. and Sprintall, J., 2008. The Indonesian Throughflow: 3-year INSTANT composite view, submitted for publication..

Heimbach, P., C. Wunsch, G. Forget, R. Ponte,2009. Controls on the Atlantic meridional volume and heat transport: magnitudes, timescales and regions, inferred from transient adjoint sensitivities, with implications for observing systems. In preparation.

Lu, Y., K. Ueyoshi, A. Köhl, E. Remy, K. Lorbacher and D. Stammer, 2002. Input Data Sets for the ECCO Global 1° WOCE Synthesis. ECCO Report No. 18, Scripps Institution of Oceanography, 37pp.

Marshall, J., Adcroft, A., Hill, C., Perelman, L. and Heisey, C., 1997. A finite-volume, incompressible Navier Stokes model for studies of the ocean on parallel computers. J. Geophys. Res, 102, 5753-5766.

McCreary, J.P. et al., 2007. Interactions between the Indonesian throughflow and circulations in the Indian and Pacific Oceans. Progress in Oceanography, 75, 70-114.

Montgomery, R. B. 1941. Sea level difference between Key West and Miami, Florida. J. Mar. Res., 4,. 32-37.

Meyers, G., 1996. Variation of Indonesian throughflow and the El Nino Southern Oscillation. J. Geophys. Res, 101,12255-12263.

Percival, D.B., Overland, J.E. and Mofjeld, H.O., 2001. Interpretation of North Pacific variability as a short- and long-memory process. Journal of Climate, 14, 4545-4559.

Percival, D. B. and A. T. Walden, 1993. Spectral Analysis for Physical Applications. Multitaper and Conventional Univariate Techniques. 583 pp, Cambridge Un. Press, Cambridge.

Potemra, J. T., and N. Schneider, 2007. Interannual variations of the Indonesian throughflow, J. Geophys. Res., 112, C05035, doi:10.1029/2006JC003808.

Ponte, R.M., Wunsch, C. and Stammer, D., 2007. Spatial mapping of time-variable errors in Jason-1 and TOPEX/Poseidon sea surface height measurements. Journal of Atmospheric and Oceanic Technology, 24, 1078-1085.

Potemra, J. T. and N. Schneider, 2007. Interannual variations of the Indonesian throughflow. J. Geophys. Res., 112, C05035, doi:10.1029/2006JC003808.

Sprintall, J., S. E. Wijffels, R. Molcard, I. Jaya, 2009: Direct estimates of the Indonesian Throughflow entering the Indian Ocean: 2004:2006. J. Geophys. Res., 114, C0700, doi:10.1029/2008JC005257.

Stammer, D., Kohl, A. and Wunsch, C., 2007. Impact of accurate geoid fields on estimates of the ocean circulation. Journal of Atmospheric and Oceanic Technology, 24, 1464-1478.

Trenberth K.,Smith, L., Qian, T., Dai, A. and Fasullo, J., 2007. Estimates of the Global Water Budget and Its Annual Cycle Using Observational and Model Data, J. Hydroclimatology, 8, 758–769

Wijffels, S.E., Meyers, G. and Godfrey, J.S., 2008. A 20-yr average of the Indonesian throughflow: Regional currents and the interbasin exchange. J. Phys. Oc. , 38, 1965-1978.

Wunsch, C. and Heimbach, P., 2006. Estimated decadal changes in the North Atlantic meridional overturning circulation and heat flux 1993-2004. J. Phys. Oc. , 36, 2012-2024.

Wunsch, C. and Heimbach, P., 2007. Practical global oceanic state estimation. Physica D-Nonlinear Phenomena, 230, 197-208.

Wunsch, C. and Heimbach, P., 2009. The Global Zonally Integrated Ocean Circulation, 1992-2006: Seasonal and Decadal Variability. J. Phys. Oc., 39, 351-368.

Wyrtki, K., 1987. Indonesian Through-flow and the associated pressure-gradient. J. Geophys. Res., 92, 12941-12946.

Figure Captions

1. The vertical and time average (not depth-weighted) misfit to 16 years of profiling float temperature data, although most of the observations (Argo) are confined to the interval since 2001. In an ideal solution, in which the expected errors were also known perfectly, the misfits would be spatial white noise obeying a χ_1^2 distribution. Some spatially systematic misfits are observed e.g. in the southeast Pacific Ocean, although whether they represent model difficulties, data calibration issues, or simply a still unconverged solution, is obscure. The misfits are dominated by the very deepest values near 2000m. Indian Ocean salinity misfits (not shown) are believed to arise primarily from calibration errors in the data. Misfits are, by definition, dimensionless.

2. Difference in meters (not squared or weighted) of the time-means of the altimetry and model solution over 16 years. This form of display shows that there are some sign-systematic differences over certain areas. In an ideal solution, the distribution should be zero-mean Gaussian white noise. Altimetric data distribution is close to globally uniform.

3. Anomaly of the Southern Oscillation Index (from NOAA website). The arrow denotes the time interval of the INSTANT measurements, and the Niño3 index maximum occurs as marked by the dashed vertical line at the end of 1997.

4. Temperature (°C) at 118m in the model in January 1992 showing the topography of the passages and the meridional sections used here. Section 1, at the western boundary, is not sub-divided; Section 2 is divided into 3 parts, with 2B being the sum of 2B′ and 2C. Subsections 3B and 4B are not discussed here.

5. Histogram of the annual mean transport values across Section 2B, U_{2B}.

6. 15-year average zonal flow in section 2B, U_{2B}, at 114.5°E (m/s). No obvious simple reference level for thermal wind calculations emerges.

7. August flow (m/s), U_{2B}, for four different years (1993, 1997, 2001, 2005) showing how variable the flow can be from year-to-year. Along the coast of Indonesia, the near-surface flow is persistently westward in August but reverses in a complicated way at depth.

8. U_{2B} (Sv) in each month across subsection 2B (upper panel). Dashed line is the running annual mean and dotted horizontal line is the temporal mean. U_{2A} (dashed) and the total, U_2 are shown in the lower panel. U_2 is almost identical to U_1 in Fig. 9. Vertical line denotes the time of the Niño3 index maximum, and the INSTANT interval is shown by the arrows.

9. Total zonal transport month-by-month across Section 1, U_1. The vertical dashed line indicates December 1997, the time of the maximum in the Niño3 index. Total transports across the remaining sections (not shown) are identical to within small volume divergences of O(0.1Sv). The time mean is 143±4Sv.

10. Power densities (upper panel) of U_{2A}, U_{2B} and of the total, U_2. U_{2B} is defined here as the ITF. The power density of the total lies between that of the two segments for most frequencies, consistent with a general compensation in the flows, with one increasing the other decreasing. Lower panel shows the integrated spectral densities normalized to a total of unity, and convenient for determining the fraction of the energy in any finite frequency band. Thus the power in the annual band contains about 50% of the variance in the ITF, but somewhat less in the sum of the ITF and SAT. These multitaper spectral estimates tend to suppress energy in the lowest frequency bands.

11. Coherence between the transports, U_{2B}, U_{2A}, in the ITF and SAT for Section 2. Note the linear frequency scale. At low frequencies, the estimated coherence is below the level-of-no-significance at approximately 95% confidence, shown as a dashed line. In the lower panel, gray bands denote the 95% confidence interval for phase. Where there is finite coherence, the phase

is indistinguishable from $\pm 180°$ as simple flow compensation between the ITF and SAT would require.

12. Time mean absolute dynamic topography in meters. η_{west}, η_{east} are the spatial averages over the two boxes.

13. Expanded version of Fig. 12. Time average absolute dynamic topography (meters, 10 cm contour interval) showing the intricate local topography of the flow. A general north-to-south pressure decrease exists but with a complex zonal and meridional structure defying easy description. Much detail exists with amplitudes below 10cm, but is uncontoured here.

14. (Upper Panel). Areal average monthly anomaly values of sea surface height η in the two boxed regions of Fig. 12. The time of the minimum in the Niño4 index is shown as a dashed line in December 1997. The large El Niño signal is visually obvious. (Lower Panel). Difference of the two mean values of η in the upper panel. Note that the Niño signal is visually obvious in η_{east}, but not apparent in η_{west}. In the difference pressure, it is apparent, but less extreme than some later events not associated with major Los Niños.

15. Coherence of the pressure difference $\eta_{EAST} - \eta_{WEST}$ with the total transport through section 2B. Strong coherence exists in the annual band, but whatever exists at lower frequencies below the level of no significance and would at most, account for 15% of the variance in that band. Gray band is the estimated 95% confidence interval for the coherence phase.

16. (Upper panel) τ_x averaged over eastern (solid) and western (dashed) regions. (Lower panel) Difference between the eastern and western wind stresses. The anomalously negative difference following the onset of El Niño corresponds to the increased westward ITF during that interval.

17. Coherence, amplitude and phase, of τ_x averaged over the eastern region, with U_{2B}.

There is strong coherence at low frequencies, near zero-phase, and also at the annual cycle and its harmonics.

18. Sensitivity of mean December U_{2B} to perturbations in the zonal wind stress τ_x in the ECCO solution. Units are Sv/Newton/hour. Each panel shows the sensitivity to a disturbance at an earlier time, at times -0.125, -0.25, -0.5 -1.0, -2.0 and -5.0 years. These charts can be interpreted in terms of the dynamics of the adjoint system (see Heimbach et al., 2009).

19. Time mean profiles of temperature in the four sections reflecting the weighting to the upper ocean involved in the temperature transports.

20. Temperature transports in °C Sv for the northern sections (upper panel) and for T_{2A} Southern Ocean (lower panel) as well as T_1. Results are very noisy, with a strong annual component, with even short-lived reversals into the Pacific possible. In the ITF, commonly a higher temperature flux comes in from the east than exists to the west through 2B. T_1,which has a strong tropical contribution differs considerably from the net south of Australia in T_{2A}. 1°C Sv$\approx 4 \times 10^{12}$W if a reference temperature of 0°C is used.

21. Divergence of the salt flux between sections 2B and 3B (solid line) and between 3B and 4B (dashed). Normalization by a salinity of 35 gives an equivalent fresh water addition of 0.029 Sv for each unit of salt flux convergence.

22. Time-mean net fresh water flux (positive into the ocean) 10^4kg/m^2/s. The region is one of intricate spatial variation in the precipitation minus evaporation pattern but is one of net precipitation in the regions north and east of the ITF.

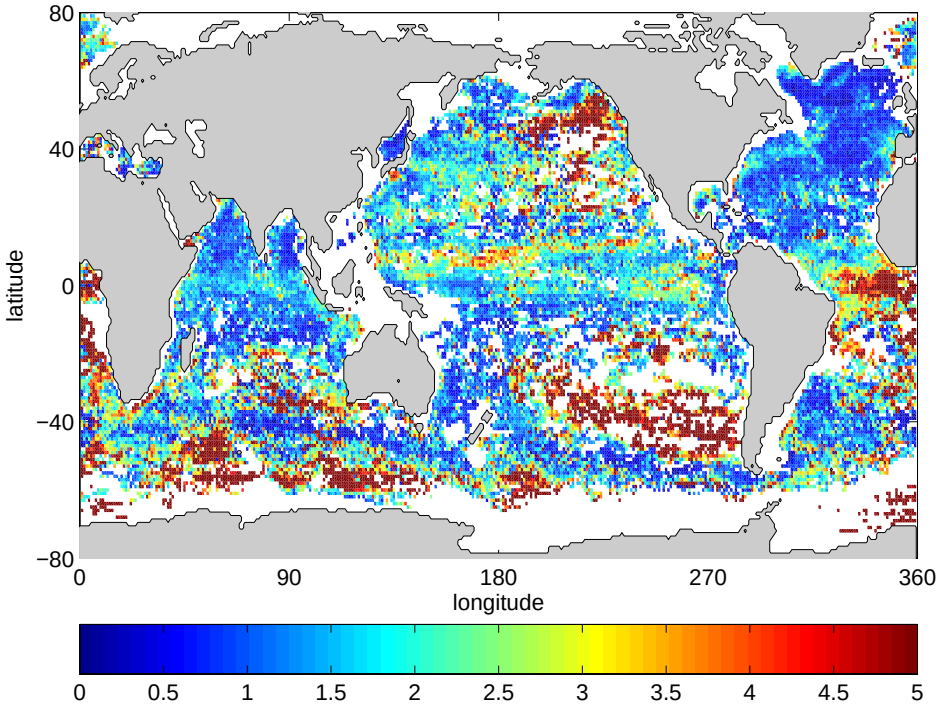

Figure 1: The vertical and time average (not depth-weighted) misfit to 16 years of profiling float temperature data, although most of the observations (Argo) are confined to the interval since 2001. In an ideal solution, in which the expected errors were also known perfectly, the misfits would be spatial white noise obeying a χ_1^2 distribution. Some spatially systematic misfits are observed e.g. in the southeast Pacific Ocean, although whether they represent model difficulties, data calibration issues, or simply a still unconverged solution, is obscure. The misfits are dominated by the very deepest values near 2000m. Indian Ocean salinity misfits (not shown) are believed to arise primarily from calibration errors in the data. Misfits are, by definition, dimensionless.

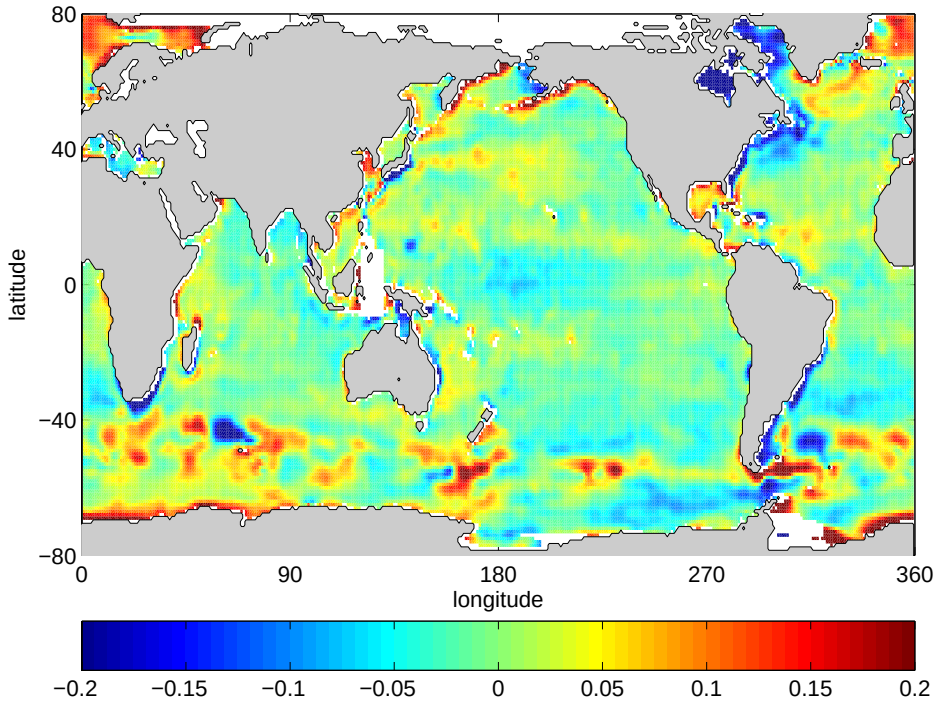

Figure 2: Difference in meters (not squared or weighted) of the time-means of the altimetry and model solution over 16 years. This form of display shows that there are some sign-systematic differences over

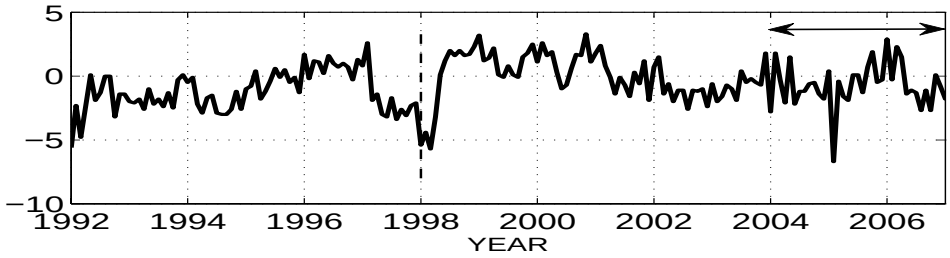

Figure 3: Anomaly of the Southern Oscillation Index (from NOAA website). The arrow denotes the time interval of the INSTANT measurements, and the Niño3 index maximum occurs as marked by the dashed vertical line at the end of 1997.

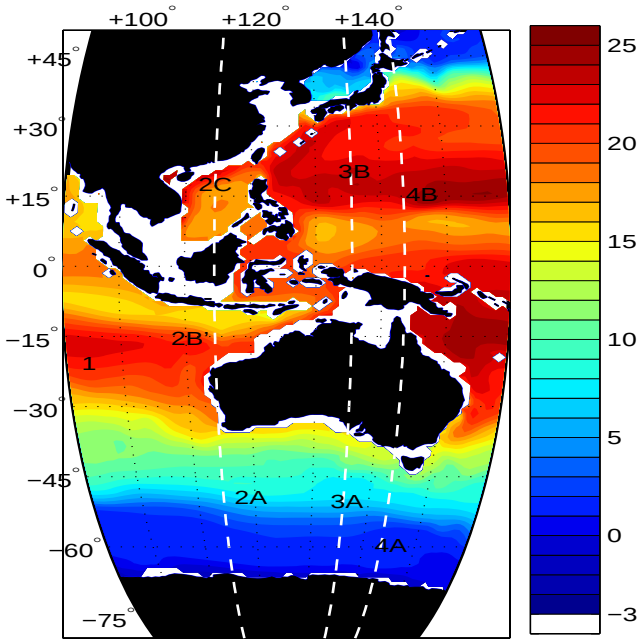

Figure 4: Temperature (°C) at 118m in the model in January 1992 showing the topography of the passages and the meridional sections used here. Section 1, at the western boundary, is not sub-divided; Section 2 is divided into 3 parts, with 2B being the sum of 2B′ and 2C. Subsections 3B and 4B are not discussed here.

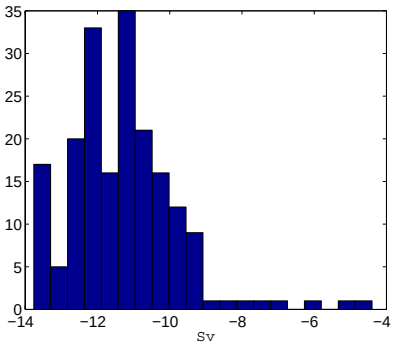

Figure 5: Histogram of the annual mean transport values across Section 2B, U_{2B}.

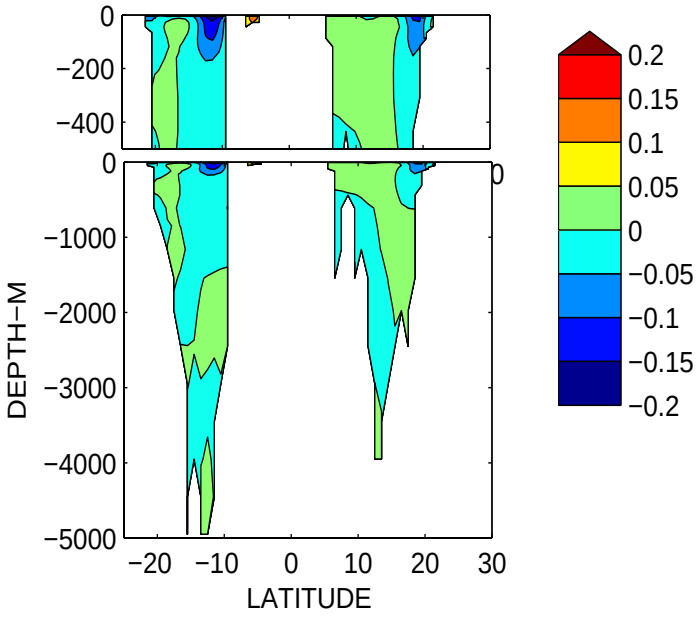

Figure 6: 15-year average zonal flow in section 2B, U_{2B}, at 114.5°E (m/s). No obvious simple reference level for thermal wind calculations emerges.

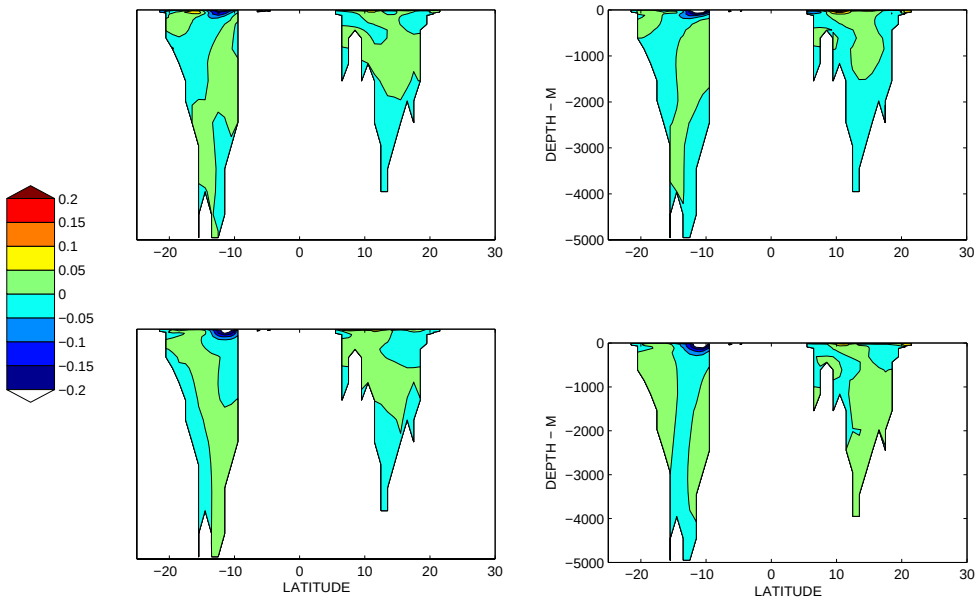

Figure 7: August flow (m/s), U_{2B}, for four different years (1993, 1997, 2001, 2005) showing how variable the flow can be from year-to-year. Along the coast of Indonesia, the near-surface flow is persistently westward in August but reverses in a complicated way at depth.

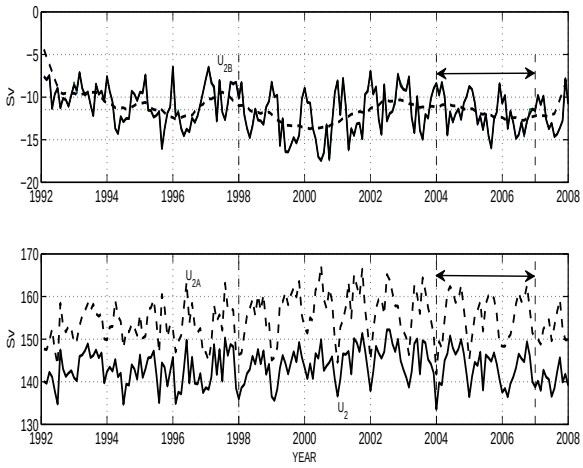

Figure 8: U_{2B} (Sv) in each month across subsection 2B (upper panel). Dashed line is the running annual mean and dotted horizontal line is the temporal mean. U_{2A} (dashed) and the total, U_2 are sh he

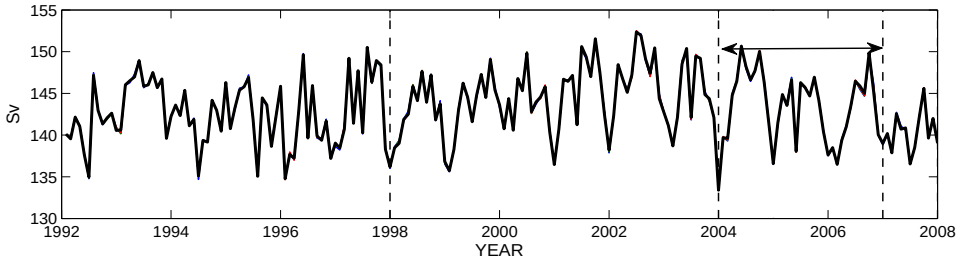

Figure 9: Total zonal transport month-by-month across Section 1, U_1. The vertical dashed line indicates December 1997, the time of the maximum in the Niño3 index. Total transports across the remaining sections (not shown) are identical to within small volume divergences of O(0.1Sv). The time mean is 143±4Sv.

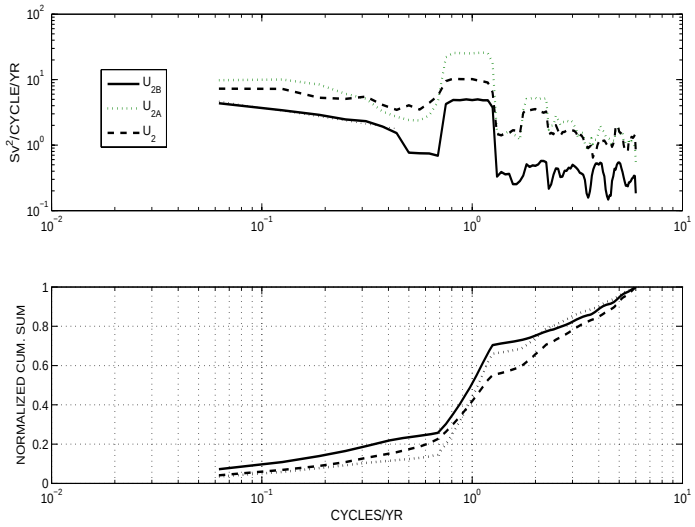

Figure 10: Power densities (upper panel) of U_{2A}, U_{2B} and of the total, U_2. U_{2B} is defined here as the ITF. The power density of the total lies between that of the two segments for most frequencies, consistent with a general compensation in the flows, with one increasing the other decreasing. Lower panel shows the integrated spectral densities normalized to a total of unity, and convenient for determining the fraction of the energy in any finite frequency band. Thus the power in the annual band contains about 50% of the variance in the ITF, but somewhat less in the sum of the ITF and SAT. These multitaper spectral estimates tend to suppress energy in the lowest frequency bands.

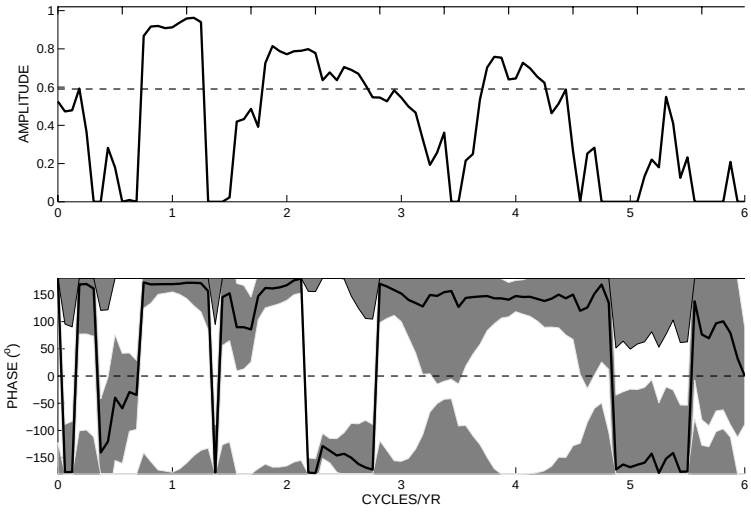

Figure 11: Coherence between the transports, U_{2B}, U_{2A}, in the ITF and SAT for Section 2. Note the linear frequency scale. At low frequencies, the estimated coherence is below the level-of-no-significance at approximately 95% confidence, shown as a dashed line. In the lower panel, gray bands denote the 95% confidence interval for phase. Where there is finite coherence, the phase is indistinguishable from $\pm 180°$ as simple flow compensation between the ITF and SAT would require.

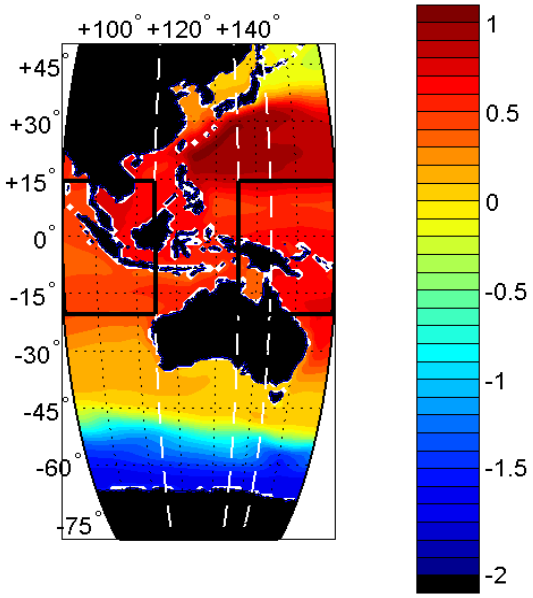

Figure 12: Time mean absolute dynamic topography in meters. η_{west}, η_{east} are the spatial averages over the two boxes.

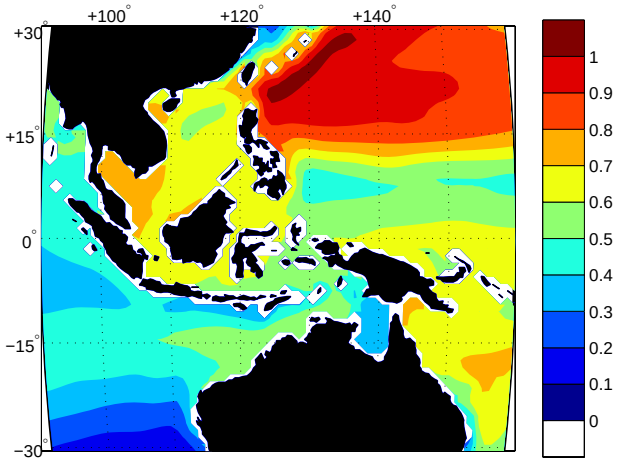

Figure 13: Expanded version of Fig. 12. Time average absolute dynamic topography (meters, 10 cm contour interval) showing the intricate local topography of the flow. A general north-to-south pressure decrease exists but with a complex zonal and meridional structure defying easy description. Much detail exists with amplitudes below 10cm, but is uncontoured here.

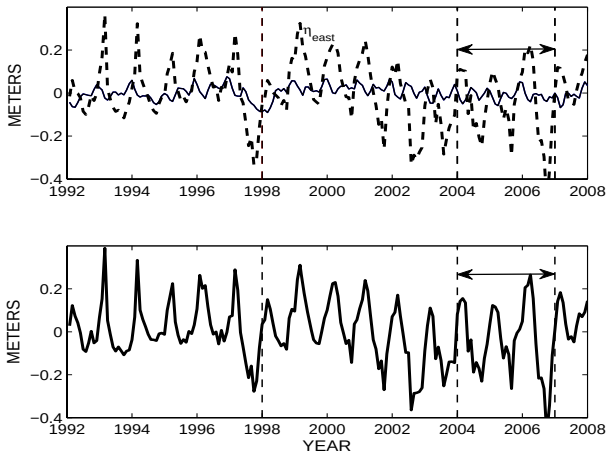

Figure 14: (Upper Panel). Areal average monthly anomaly values of sea surface height η in the two boxed regions of Fig. 12. The time of the minimum in the Niño4 index is shown as a dashed line in December 1997. The large El Niño signal is visually obvious. (Lower Panel). Difference of the two mean values of η in the upper panel. Note that the Niño signal is visually obvious in η_{east}, but not apparent in η_{west}. In the difference pressure, it is apparent, but less extreme than some later events not associated with major Los Niños.

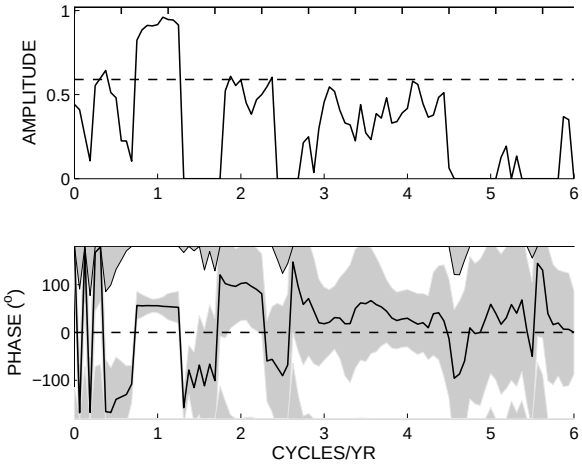

Figure 15: Coherence of the pressure difference $\eta_{EAST} - \eta_{WEST}$ with the total transport through section 2B. Strong coherence exists in the annual band, but whatever exists at lower frequencies below the level of no significance and would at most, account for 15% of the variance in that band. Gray band is the estimated 95% confidence interval for the coherence phase.

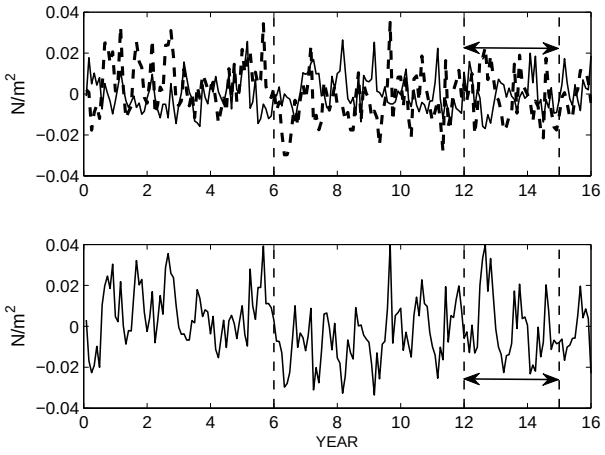

Figure 16: (Upper panel) τ_x averaged over eastern (solid) and western (dashed) regions. (Lower panel) Difference between the eastern and western wind stresses. The anomalously negative difference following the onset of El Niño corresponds to the increased westward ITF during that interval.

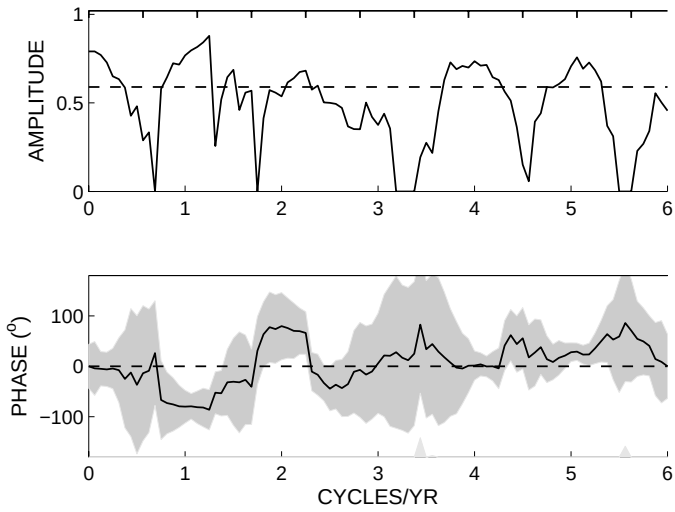

Figure 17: Coherence, amplitude and phase, of τ_x averaged over the eastern region, with U_{2B}. There is strong coherence at low frequencies, near zero-phase, and also at the annual cycle and its harmonics.

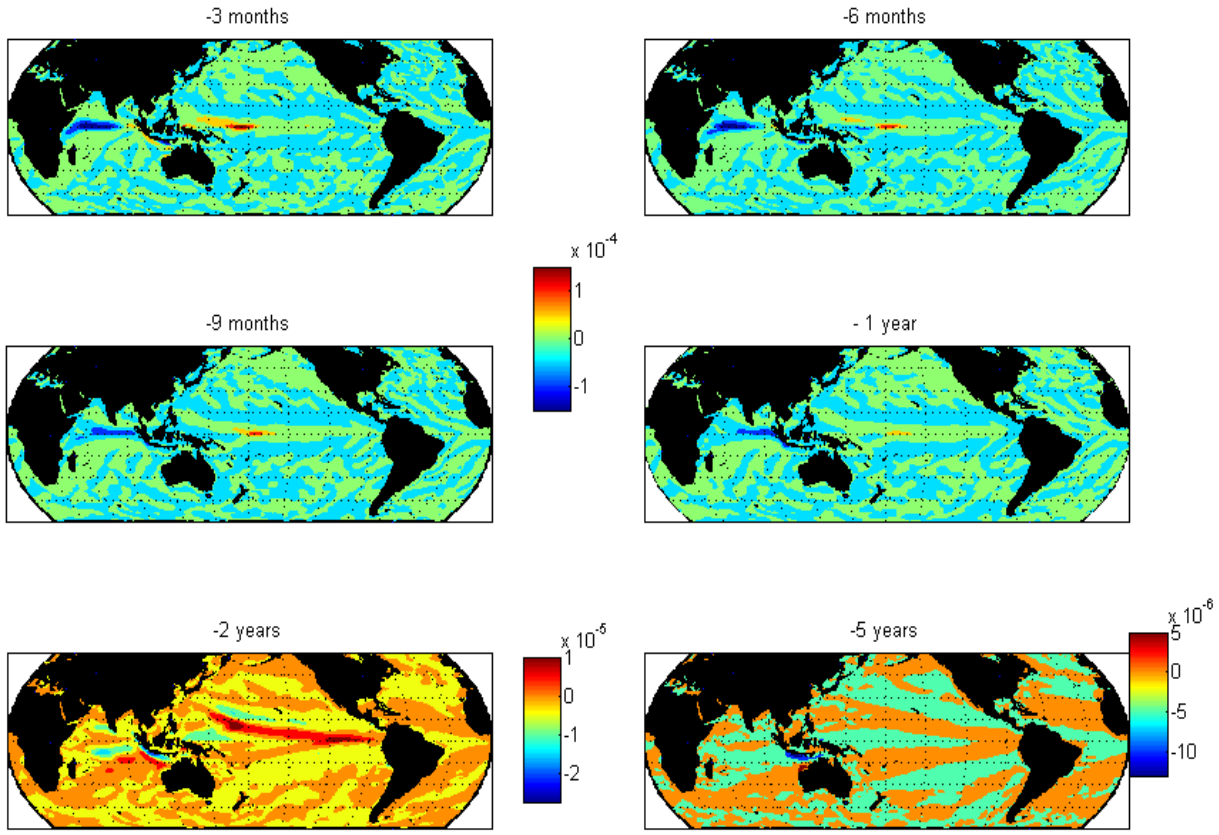

Figure 18: Sensitivity of mean December U_{2B} to perturbations in the zonal wind stress τ_x in the ECCO solution. Units are Sv/Newton/hour. Each panel shows the sensitivity to a disturbance at an earlier time, at times -0.125, -0.25, -0.5 -1.0, -2.0 and -5.0 years. These charts can be interpreted in terms of the dynamics of the adjoint system (see Heimbach et al., 2009).

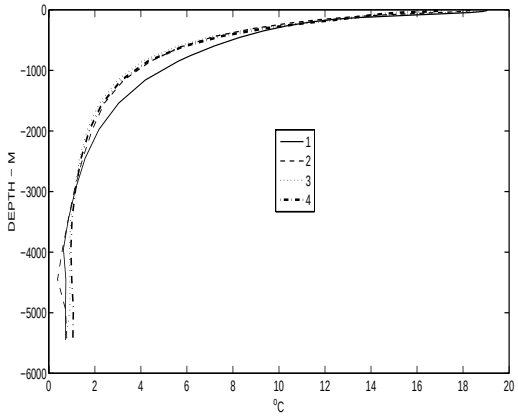

Figure 19: Time mean sections of temperature in the four sections reflecting the weighting to the upper ocean involved in the temperature transports.

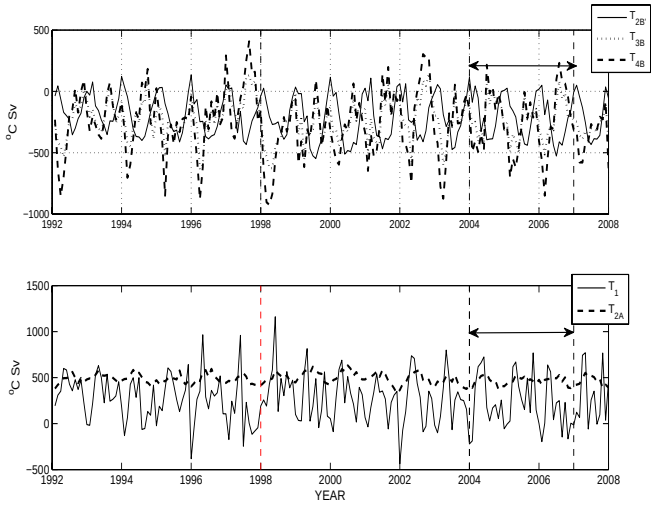

Figure 20: Temperature transports in °C Sv for the northern sections (upper panel) and for T_{2A} Southern Ocean (lower panel) as well as T_1. Results are very noisy, with a strong annual component, with even short-lived reversals into the Pacific possible. In the ITF, commonly a higher temperature flux comes in from the east than exists to the west through 2B. T_1,which has a strong tropical contribution differs considerably from the net south of Australia in T_{2A}. 1°C Sv$\approx 4 \times 10^{12}$W if a reference temperature of 0°C is used.

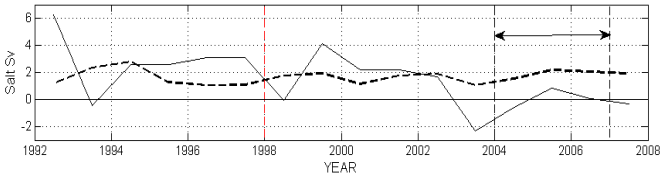

Figure 21: Divergence of the salt flux between sections 2B and 3B (solid line) and between 3B and 4B (dashed). Normalization by a salinity of 35 gives an equivalent fresh water addition of 0.029 Sv for each unit of salt flux convergence.

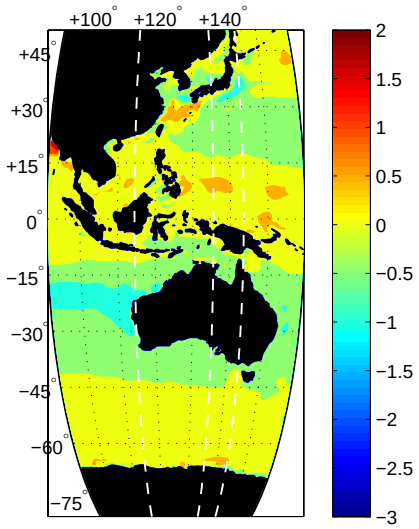

Figure 22: Time-mean net fresh water flux (positive into the ocean) $10^4 \mathrm{kg/m^2/s}$. The region is one of intricate spatial variation in the precipitation minus evaporation pattern but is one of net precipitation in the regions north and east of the ITF.